1   **Revision 3**

2

3   **Topotactic and reconstructive changes at high pressure and**

4   **temperatures from Cs-natrolite to Cs-hexacelsian**

5   Huijeong Hwang,[1] Donghoon Seoung,[1] G. Diego Gatta,[2] Douglas A. Blom,[3]

6   Thomas Vogt,[3] Yongjae Lee[1], *

7

8   [1]Department of Earth System Sciences, Yonsei University, Seoul 120-749, Korea

9   [2]Dipartimento di Scienze della Terra, Università degli Studi di Milano, Via Botticelli, 23,
10   I-20133 Milano, Italy

11   [3]NanoCenter & Department of Chemistry and Biochemistry, University of South
12   Carolina, Columbia, SC 29208, USA

13

14   **Abstract**

15   Synchrotron X-ray powder diffraction experiments have been performed on dehydrated

16   Cs-exchanged natrolite in order to systematically investigate successive transitions under

17   high pressures and temperatures. At pressures above 0.5(1) GPa using H_2O as a pressure

18   transmitting medium and after heating to 100 °C, dehydrated $Cs_{16}Al_{16}Si_{24}O_{80}$ (deh-Cs-

19   NAT) transforms to a hydrated phase $Cs_{16}Al_{16}Si_{24}O_{80} \cdot 16H_2O$ (Cs-NAT-II), which has a ca.

20   13.9% larger unit-cell volume. Further compression and heating to 1.5 GPa and 145 °C

21   results in the transformation of Cs-NAT-II to $Cs_{16}Al_{16}Si_{32}O_{96}$ (anh-Cs-POL), a H_2O-free

22   pollucite-like triclinic phase with a 15.6% smaller unit-cell volume per 80 framework

23   oxygen atoms ($80O_f$). At pressures and temperatures of 3.7 GPa and 180 °C, a new phase

24   $Cs_{1.547}Al_{1.548}Si_{6.452}O_{16}$ (Cs-HEX) with a hexacelsian framework forms, which has a ca.

25   1.8% smaller unit-cell volume per $80O_f$. This phase can be recovered after pressure

26   release.   The structure of the recovered Cs-HEX has been refined in space group

27    $P6_3/mcm$ with a = 5.3731(2) Å and c = 16.6834(8) Å, and also been confirmed by

28   HAADF-STEM real space imaging. Similar to the hexacelsian feldspar (*i.e.* $BaAl_2Si_2O_8$),

29   Cs-HEX contains Cs^+ cations which act as bridges between the upper and lower layers

30   composed of tetrahedra and are hexa-coordinated to the upper and lower 6-membered

31   ring windows. These pressure- and temperature-induced reactions from a zeolite to a

32   feldspar-like material are important constraints for the design of materials for Cs^+

33   immobilization in nuclear waste disposal.

34

35   **Keywords** : Natrolite, Hexacelsian, High-pressure, Phase transition, X-ray powder

36   diffraction, Radioactive wastes.

37

38

Introduction

40   Natrolite   (ideally $Na_{16}Al_{16}Si_{24}O_{80} \cdot 16H_2O$,   Na-NAT)   is   a   small   pore

41   aluminosilicate mineral that has been characterized in the early 1930s as a member of the

42   "fibrous zeolites" group, with a framework composed of T_5O_{10} tetrahedral units (Pauling

43   1930 and Taylor et al. 1933).   Although natrolite forms in many hydrothermal

44   environments (Klaproth, M.H. 1803), technological applications for it have been limited

45   as its pores are small (~2.6 Å) and filled with strongly bonded Na^+-H_2O clusters (Baur et

46   al. 1990). However, it has recently been demonstrated that after exchanging Na^+ by K^+,

47   these ordered Na^+-H_2O cluster rearrange into disordered K^+-H_2O ones concomitant with a

2

48   ~ 10% expansion of the unit-cell volume (Lee et al. 2010, 2013). Subsequently, facile ion

49   exchange of K^+ by Rb^+-, Cs^+-, Ca^{2+}-, Sr^{2+}-, Ba^{2+}-, Cd^{2+}-, Pb^{2+}-, and Ag^+ as extra-

50   framework cations (EFC) is possible using traditional solution exchange methods, thus

51   defying the notion that natrolite is only a "soda-stone" (Lee et al. 2011).

52   Natrolite has also been shown to undergo intriguing structural changes under

53   hydrostatic pressure. When compressed using hydrous liquids as pressure transmitting

54   media, the unit-cell volume of natrolite expands by ca. 7% at 1 GPa while it adsorbs H_2O

55   into its pores and forms $Na_{16}Al_{16}Si_{24}O_{80} \cdot 24H_2O$ (Lee et al. 2005). It subsequently

56   contracts by ca. 5% at 1.2 GPa while continuing to adsorb H_2O and forms a 'super-

57   hydrated' zeolite $Na_{16}Al_{16}Si_{24}O_{80} \cdot 32H_2O$ (Lee et al. 2005). Super-hydration in natrolite

58   occurs *via* cooperative rotations and anti-rotations of the T_5O_{10} tetrahedral units which

59   increase the pore H_2O content by 50% at 1 GPa and 1.2 GPa, respectively, while the

60   framework remains intact. This has been coined "pressure-induced hydration (PIH)" and

61   found to be a general property of the natrolite framework depending on the type of EFC

62   being present (Gatta 2005; Seoung et al. 2013; Gatta and Lee 2014). The observed unit-

63   cell volume expansion is inversely related to the size of the EFC: Li^+-exchanged natrolite

64   exhibits the largest volume expansion of ca. 20.6(1)% while doubling its H_2O content

65   near 1 GPa, whereas Rb^+-exchanged natrolite super-hydrates near 2 GPa, while

66   undergoing only a minute unit-cell volume expansion of 0.3(1)% when doubling its H_2O

67   content (Seoung et al. 2013). Grima et al. (2007) showed that natrolite is an auxetic

68   zeolite, having negative Poisson's ratios and thus being able to contract perpendicular to

69   the direction it is being compressed (Grima et al. 2007). Using density functional theory

70   (DFT), the auxetic properties of natrolites containing monovalent EFC could be modeled

71   and, furthermore, it was proposed that Cs-natrolite which does not undergo any PIH (but

72   only a volume contraction of ca. 4.8% near 0.3 GPa) transforms under pressure by the

73   Cs^+ cations moving to neighboring channels (Kremleva et al. 2013). This volume

74   contraction results in significant changes of the disordered Cs^+-H_2O topology within the

75   channels as a 90° rotation of the Cs^+ ions is concomitant with a 45° rotational ordering of

76   the H_2O ligands when compared to the low pressure Cs-NAT-I phase. In addition, the

77   high-pressure, high-density phase, called Cs-NAT-II, is found to be about three times

78   more compressible than Cs-NAT-I.

79   We have recently found that further densification can be induced by heating Cs-

80   NAT-II. At 1.5 GPa and 145 °C, Cs-NAT-II transforms to a pollucite-related, highly

81   dense, and H_2O-free triclinic phase with the nominal composition $CsAlSi_2O_6$. This is an

82   irreversible phase transition going from $Cs_{16}Al_{16}Si_{24}O_{80} \cdot 16H_2O$ to $Cs_{15}Al_{15}Si_{30}O_{80}$ which

83   involves reconstructive changes of the framework (Im et al. 2014). After pressure release,

84   this anhydrous pollucite-related phase is recovered as a monoclinic phase. The

85   significant heat load caused by both nuclear decay and electron self-radiation in materials

86   containing ^{137}Cs and ^{90}Sr during the early stages of nuclear waste disposal, calls for their

87   separation from the waste stream and will significantly increase the storage capacity of

88   high-level nuclear waste and reduce costs while complying with regulatory requirements.

89   Due to its chemical stability and high Cs-loading of 42.6 weight-%, the aluminosilicate

90   pollucite ($CsAlSi_2O_6 \cdot H_2O$) has been identified as a preferred nuclear waste form for Cs

91   (Gatta et al. 2009a, 2009b, Sanchez-Valle et al. 2010). In most cases, a multi-step process

92   starting with CsOH is used to prepare a sol which is then hydrothermally treated at

93   temperatures close to 200 °C to end up with a dry pollucite powder (MacLaren et al.

94   1999).

95   In this paper, we report that further pressure- and heat-treatment of the triclinic

96   pollucite-related phase results in another reconstructive phase transformation from

97    $Cs_{15}Al_{15}Si_{30}O_{80}$ to a more silicon-rich hexacelsian-related phase with composition

98    $Cs_{7.74}Al_{7.74}Si_{32.26}O_{80}$. We have performed combined *in situ* high-pressure and *ex situ*

99   high-temperature synchrotron X-ray powder diffraction and high angle annular dark field

100   scanning transmission electron microscopy (HAADF-STEM) real space imaging and

101   established the complete pathway of the successive structural phase transformations from

102   dehydrated Cs-exchanged natrolite (deh-Cs-NAT) *via* its hydrated high-pressure phase

103   (Cs-NAT-II) and the anhydrous pollucite-related triclinic phase (anh-Cs-POL), and finally

104   to the hexacelsian-related phase (Cs-HEX) which forms above 3.7 GPa and at 180 °C.

105   Rietveld structural refinements reveal that the recovered hexacelsian-like phase is ca. 8.4%

106   less dense than the original Cs-NAT-I.

107

108   **Experimental Section**

109   **- Sample preparation and synchrotron X-ray powder diffraction**

110   The preparation of Cs-exchanged natrolite (Cs-NAT-I) and its dehydrated form (deh-Cs-

111   NAT) is described in detail by Lee et al. (2010) and Lee et al. (2011). *In situ* high-

112   pressure synchrotron X-ray powder diffraction was performed using a Merrill-Bassett

113   type diamond-anvil cell (DAC) at the X14A beamline at the National Synchrotron Light

114   Source (NSLS) at Brookhaven National Laboratory (BNL). The primary white beam

115   from a bending magnet was horizontally monochromatized by Si (111) double crystals to

116   produce monochromatic X-ray with wavelength of 0.7745 Å. The powder sample was

5

117   loaded into a 410μm diameter - 110μm thick sample chamber in a pre-indented stainless

118   steel gasket. A few small ruby spheres were used as *in situ* pressure markers inside the

119   sample chamber. Distilled water was used as a pore-penetrating pressure-transmitting

120   medium (PTM). After applying the PTM to the sample, the DAC was quickly sealed to

121   the first measured pressure point. The pressure at the sample was measured by detecting

122   R_1 emission line of the included ruby spheres in the DAC (Mao et al. 1986). Pressure

123   was increased up to 4.32 GPa at step intervals of ca. 0.25 GPa. *Ex situ* heat treatment

124   was occasionally applied by placing the DAC inside an oven for a few hours to induce

125   hydrostatic conditions of the PTM at respective pressures. Errors in pressure and

126   temperature measurements are estimated to be ±0.1 GPa and ±10°C, respectively. The *in*

127   *situ* pressure and *ex situ* heat treatment sequences are summarized in Table 1 along with

128   the resulting changes in the unit-cell volume and calculated density.

129

130   **- Rietveld structure refinement**

131   Structural refinements of the recovered hexacelsian-like phase, Cs-HEX, formed at 3.7

132   GPa after heating at 180 °C were performed by Rietveld methods using GSAS and

133   EXPGUI (Larson and Von Dreele 1986; Toby 2001).   The background curve was fitted

134   with a Chebyshev polynomial. The pseudo-Voigt profile function proposed by Thompson

135   et al. (1987) was used to fit the observed peaks. The starting framework model used was

136   that of the Ba-hexacelcian ($P6_3$/mcm) by Kremenovic et al. (2003). The tetrahedral site

137   (T-site) was assumed to be statistically occupied by Si and Al atoms. An inspection of the

138   difference-Fourier map of the electron density suggested that the Cs was located at the

139   extra-framework 2*b* (0,0,0) site. The refined occupancy of the Cs cation was then used to

6

140   fix the Al occupancy at the disordered T-site.   Geometrical soft restraints were applied on

141   the disordered T-site based on the fixed occupancies of $Si_{0.81}$ and $Al_{0.19}$; T-O and O-O

142   inter-atomic distances of the tetrahedra were restrained to target values of 1.635 ± 0.001

143   Å, and 2.669 ± 0.005 Å, respectively.   To reduce the number of parameters, all the atoms

144   were modeled with one isotropic displacement parameters (U_{iso}).   Preferred orientation

145   along [00l] directions were taken into account and corrected for.   Scanning transmission

146   electron microscopy imaging revealed that the crystallites are thin platelets perpendicular

147   to the [001] direction (see Figure 5).   Reflections with d-spacing along the [001] direction

148   are therefore statistically under-sampled in a powder experiment and appropriate

149   preferred orientation corrections need to be applied.   Preferred orientation function by

150   March-Dollase (Dollase 1986) was used, and the <001> component were refined, on

151   average, to 1.076.   In the final stage of the refinements, the weights of the soft restraints

152   were reduced, which did not result in any significant changes of the inter-atomic

153   distances.   The final convergence of the refinement was achieved by varying

154   simultaneously all background and profile parameters, preferred orientation parameters,

155   scale factor, lattice constants, 2θ zero, and the atomic positional and displacement

156   parameters. The results of the final refined models are summarized in Tables 2, 3 and 4.

157

158   **- Imaging using High Angle Annular Dark Field Scanning Transmission Electron**

159   **Microscopy**

160   Scanning transmission electron microscopy was used to image the atomic arrangements

161   of the recovered Cs-HEX particles using a JEOL 2100F 200kV FEG-STEM/TEM

162   equipped with a CEOS Cs corrector on the illumination system. High angle annular dark-

7

163   field STEM images were acquired on a Fischione Model 3000 HAADF detector with a

164   camera length such that the inner cut-off angle of the detector was 75 mrad. The acquired

165   real space images are shown in Fig. 5.

166

167

168   **Results and Discussion**

169   The changes in the synchrotron X-ray powder diffracttion patterns at respective

170   pressures and temperatures show successive transformations from deh-Cs-NAT to Cs-

171   HEX (Fig. 1). Above 0.5 GPa and 100 °C, deh-Cs-NAT (*i.e.,* $Cs_{16}Al_{16}Si_{24}O_{80}$) transform

172   to the hydrated phase, Cs-NAT-II (*i.e.,* $Cs_{16}Al_{16}Si_{24}O_{80} \cdot 16H_2O$) *via* pressure-induced

173   hydration. The insertion of H_2O molecules from the PTM into the natrolite channels

174   causes the expansion of the unit-cell volume by ca. 13.9% (Table 1, Fig. 2). As a result,

175   the density of Cs-NAT-II decreases by c.a. 6.5% compared to deh-Cs-NAT at 0.5 GPa. In

176   Cs-NAT-II, the Cs^+ cations migrate towards the middle of the channel as the H_2O

177   molecules occupy the wall sites of the channel (Fig. 3). The amount of H_2O molecules

178   inserted under pressure is 16 per $80O_f$, which is the same as in the original Cs-exchanged

179   natrolite (Seoung et al. 2013). The Cs^+-H_2O cluster in Cs-NAT-II are in an ordered

180   arrangement with fully occupied cation and H_2O sites, unlike the statistically-distributed

181   model in the original Cs-exchanged natrolite. As the DAC is annealed at 145 °C and 1.5

182   GPa, Cs-NAT-II transforms partially to a triclinic H_2O-free pollucite-like phase

183    $Cs_{16}Al_{16}Si_{32}O_{96}$ (anh-Cs-POL). This leads to the contraction of the unit-cell volume by

184   ca. 15.6% per $80O_f$ (Table 1, Fig. 2). While the initial pressure-induced hydration is

185   topotactic with respect to the framework and facilitated by an opening of the pores due to

                                                                                    8

186 the auxetic properties of this framework (Grima et 1l 2007, Kremleva et al 2013, Seoung

187 et al 2013), the dehydration at 0.5 GPa and 100 °C leads to a reconstruction of the

188 framework accompanied by Cs and Al leaching.

189   Further increase in pressure to 2.6 GPa leads to a complete conversion of Cs-

190 NAT-II into anh-Cs-POL persisting up to 3.7 GPa. After heating at 180°C, anh-Cs-POL

191 transforms to a new hexagonal phase, with a hexacelsian-like framework in $P6_3$/mcm.

192 This hexacelsian-like phase, *i.e.* Cs-HEX, was observed up to the final pressure of 4.3

193 GPa and is recovered after pressure release (Figs. 1 and 2). The unit-cell volume of the

194 recovered Cs-HEX is ca. 6.7% smaller than that of the starting deh-Cs-NAT per 80O$_f$ and

195 therefore about 9.0% smaller than that of the original Cs-NAT-I, respectively, at ambient

196 conditions. The overall pressure- and temperature-induced transformations are illustrated

197 in Fig. 3.

198   The structural model of Cs-HEX was derived from Rietveld structural

199 refinements using synchrotron X-ray powder diffraction data collected under pressure and

200 after pressure release (Table 2, 3 and 4; Fig. 4). Similar to the Ba-hexacelsian structure,

201 the refined structure of Cs-HEX is composed of double sheets of disordered Si/Al

202 tetrahedra on the plane perpendicular to the *c*-axis. Each double sheet consists of

203 upward- and downward-oriented TO$_4$ tetrahedral sub-layers bridged by O1 oxygen hinges

204 with T-O1-T angles of 180° (Table 4). Within each sub-layer, O2 oxygen hinges bridge

205 the individual tetrahedra with T-O2-T angle in the range between 140.3(1)° and 141.4(2)°.

206 This is larger than observed in the Ba-hexacelsian structure (Fig. 4). Cs-HEX contains

207 Cs$^+$ cations located at the 2*b* (0,0,0) sites between the double sheets of tetrahedra, with

208 interlayer distances in the range between 3.306(6) Å and 3.897(1) Å. In contrast to fully

9

209   occupied of Ba^{2+} sites in Ba-hexacelsian, the refined occupancy of Cs^+ cation is 0.773(6)

210   which results to 1.5(1) Cs atoms per unit-cell. In fact, when refined, the Al/Si ratio

211   converges to ca. 0.24(1) or 1.5(1) Al atoms per unit-cell, which matches the amount of

212   Cs^+ cations needed for electro-neutrality. We therefore propose the chemical formula of

213   Cs-HEX to be $Cs_{1.55}Al_{1.55}Si_{6.45}O_{16}$. The decrease in the Al/Si ratio from the starting phase,

214   *i.e.* 0.67 in Cs-natrolite, could be due to a phase separation and the formation of minor,

215   yet uncharacterized and highly disordered phases of aluminum and cesium, which might

216   be the reason for broad humps observed in the diffraction patterns (Fig. 1). In Cs-HEX,

217   the Cs^+ cations are coordinated by 12 oxygen atoms, *i.e.* six O2 atoms from the upper and

218   the other six from the bottom layer with interatomic distances in the range between

219   3.326(1) Å and 3.311(1) Å (Fig. 4). In Ba-hexacelsian, Ba^{2+} is hexa-coordinated by three

220   O2 oxygen atoms from the upper and the bottom layer each with interatomic distance of

221   3.052 Å and hexa-coordination at 3.151 Å. To a first approximation the contrast of

222   atomic columns imaged using HAADF-STEM varies with Z^2, Z being the atomic number

223   of the element. The unique Cs^+ arrangement in the Cs-HEX structure is observed in

224   HAADF-STEM real space images measured from recovered Cs-HEX particles as shown

225   in Fig. 5 where the bright spots indicate the position of the Cs^+ ions. Having both Ba- and

226   Cs-HEX structurally well characterized might help to model chemical and structural

227   changes occurring during the decay of $^{137}Cs^+$ under β- and γ- emissions to $^{137}Ba^{2+}$,

228   changing the cation valence and ionic radius. Further experimental findings in this field

229   have been reported by Jiang and Van Ginhoven (2012).

230

231   **Implications**

10

232   The experimental findings of this study open a new window on the behavior of

233   Cs-bearing open-framework aluminosilicates in response to pressure and temperature. A

234   *P/T*-induced densification process was observed from a Cs-bearing zeolite (with NAT

235   topology) to a Cs-hexacelsian, through a series of phase transformations toward a final

236   product which survives at room conditions.   The mechanisms of *P/T*-induced

237   densification of crystalline materials are the basis to understand the mineralogical

238   processes under extreme conditions, but in this case the main implications of the

239   experimental findings extend to nuclear technology. Pollucite-like materials have been

240   considered among the most stable Cs-bearing aluminosilicates for the inertization of Cs-

241   rich nuclear wastes. The high Cs-content of approximately 40 weight% in pollucite

242   exceeds that of any Cs-containing glass ceramics or zeolites (Donald et al. 1997).

243   Furthermore, the Cs leaching rate indicates that this material might be used for long term

244   storage of ^{137}Cs at ambient conditions (Yanagisawa et al. 1987). We deemed it important

245   to further explore the high-temperature and high-pressure chemistry of the new pollucite-

246   related phase obtained by the *P/T*-treatment of Cs-natrolite, in order to assess processes

247   which might affect its use. We show here that by increasing pressure and temperature

248   another dense phase exists, namely Cs-hexacelsian which contains less Cs per formula

249   unit than pollucite.   The reconstructive phase transition from the anhydrous triclinic

250   pollucite phase to Cs-hexacelsian results in the precipitation of Cs^+ and $Al^{3+}$and therefore

251   these pressure and temperature conditions need to be avoided if the storage of radioactive

252   Cs^+ is targeted.

253

254   **Acknowledgments**

264

265

266   **References**

267   Baur, W.H., Kassner, D., Kim, C.-H., and Sieber, N.H.W. (1990) Flexibility and

268   distortion of the framework of natrolite: crystal structures of ion-exchanged natrolites.

269   European Journal of Mineralogy, 2, 761-769.

270   Dollase, W. A. (1986) Correction of intensities for preferred orientation in

271   powder diffractometry: application of the March model. Journal of Applied

272   Crystallography, 19, 267-272.

273   Gatta, G.D. (2005) A comparative study of fibrous zeolites under pressure.

274   European Journal of Mineralogy, 17, 411-421.

275   Gatta, G.D., and Lee, Y. (2014) Zeolites at high pressure: A review.

276   Mineralogical Magazine, 78, 267-291.

277   Gatta, G.D., Rinaldi, R., McIntyre, G.J., Nénert, G., Bellatreccia, F., Guastoni, A.,

12

278   and Della Ventura G. (2009a) On the crystal structure and crystal chemistry of pollucite,

279   $(Cs,Na)_{16}Al_{16}Si_{32}O_{96}\cdot nH_2O$: a natural microporous material of interest in nuclear

280   technology. American Mineralogist, 94, 1560-1568.

281   Gatta, G.D., Rotiroti, N., Boffa Ballaran, T., Sanchez-Valle, C., and Pavese, A.

282   (2009b) Elastic behavior and phase-stability of pollucite, a potential host for nuclear

283   waste. American Mineralogist, 94, 1137-1143.

284   Grima, J.N., Gatt, R., Zammit, V., Williams, J.J., Evans, K.E., Alderson, A., and

285   Walton, R. I. (2007) Natrolite: A zeolite with negative Poisson's ratios. Journal of Applied

286   Physics, 101, 086102

287   Im, J.-H., Seoung, D., Lee, S.Y., Blom, D.A., Kao, C.C., Vogt, T., and Lee, Y.

288   (2014) Pressure-induced metathesis reaction to sequester Cs. Environmental Science &

289   Technology, online published

290   Jiang, W., and Van Ginhoven, R.M. (2012) Chemical and Charge Im-balance

291   Induced by Radionuclide Decay: Effects on Waste Form Structure. Pacific Northwest

292   National Laboratory (PNNL), Richland, WA (US), Environmental Molecular Sciences

293   Laboratory (EMSL) PNNL-20312-3

294   Klaproth, M.H. (1803) Ges. Naturforsch. Freunde Berlin, Neue Schrifl, 4, 243-

295   248.

296   Kremenović, A., Colomban, P., Piriou, B., Massiot, D., and Florian P. (2003)

297   Structural and spectroscopic characterization of the quenched hexacelsian. The Journal of

298   Physics and Chemistry of Solids, 64(11), 2253-2268.

299   Kremleva, A., Vogt, T., and Rösch, N. (2013) Monovalent cation-exchanged

300   natrolites and their behavior under pressure. A computational study. Journal of Physical

13

301   Chemistry C, 117(37), 19020-19030.

302   Larson, A., and Von Dreele, R.B. (1986) GSAS : General Structure Analysis

303   System. Los Alamos National Laboratory, New Mexico, Report LAUR, 86-748.

304   Lee, Y., Hriljac, J.A., Parise, J. B., and Vogt, T. (2005) Pressure-induced

305   stabilization of ordered paranatrolite: A new insight into the paranatrolite controversy.

306   American Mineralogist, 90(1), 252-257.

307   Lee, Y., Seoung, D., Jang, Y.N., Vogt, T., and Lee, Y. (2013) Role of Cation–

308   Water Disorder during Cation Exchange in Small-Pore Zeolite Sodium Natrolite. The

309   Journal of Physical Chemistry C, 117(31), 16119-16126.

310   Lee, Y., Lee, Y., and Seoung, D. (2010) Natrolite may not be a "soda-stone"

311   anymore: Structural study of fully K-, Rb-, and Cs-exchanged natrolite. American

312   Mineralogist, 95(11-12), 1636-1641.

313   Lee, Y., Seoung, D., and Lee, Y. (2011) Natrolite is not a "soda-stone" anymore:

314   Structural study of alkali (Li^+), alkaline-earth (Ca^{2+}, Sr^{2+}, Ba^{2+}) and heavy metal (Cd^{2+},

315   Pb^{2+}, Ag^+) cation-exchanged natrolites. American Mineralogist, 96(11-12), 1718-1724.

316   Pauling, L. (1930) The structure of some sodium and calcium aluminosilicates.

317   Proceedings of the National Academy of Sciences of the United States of America, 16(7),

318   453-459.

319   Sanchez-Valle, C., Chi-Hong, C., and Gatta, G.D. (2010) Single-crystal elastic

320   properties of $(Cs,Na)AlSi_2O_6 \bullet H_2O$ pollucite: with potential use for long-term storage of

321   Cs radioisotopes. Journal of Applied Physics, 108, 093509 (1-7).

322   Seoung, D., Lee, Y., Kao, C.C., Vogt, T., and Lee, Y. (2013) Super-hydrated

323   zeolites: Pressure-induced hydration in natrolites. Chemistry-A European Journal, 19(33),

14

324   10876-10883.

325   Taylor, W.H., Meek, C.A., and Jackson, W.W. (1933) The structures of the

326   fibrous zeolites. Zeitschrift für Kristallographie, 84(1), 373-398.

327   Thompson, P., Cox, D.E., and Hastings, J.B. (1987) Rietveld refinement of

328   Debye-Scherrer synchrotron X-ray data from Al_2O_3. Journal of Applied Crystallography,

329   20(2), 79-83.

330   Toby, B.H. (2001) EXPGUI, a graphical user interface for GSAS. Journal of

331   Applied Crystallography, 34(2), 210-213.

332   Yanagisawa, K., Nishioka, M., and Yamasaki, N.J. (1987) Immobilization of

333   cesium into Pollucite structure by hydrothermal hot-pressing. Journal of Nuclear Science

334   and Technology, 24(1), 51-60.

335

15

336   **Figure Captions**

337

338   **Figure 1.** Synchrotron X-ray powder diffraction patterns of dehy-Cs-NAT at ambient

339   (bottom) and under increasing pressure conditions. Temperatures indicate *ex situ* heating

340   before the measurement. Top pattern shows Rietveld fit of Cs-HEX with difference curve

341   (blue line) between the observed (black crosses) and calculated (red line) patterns.

342

343   **Figure 2.** (a) Pressure- and heat-induced changes in the unit-cell volumes, normalized to

344   80 framework oxygen atoms ($80O_f$) of dehydrated Cs-exchanged natrolite (deh-Cs-NAT),

345   ordered hydrated natrolite (Cs-NAT-II), H_2O-free pollucite-like phase (anh-Cs-POL), and

346   the hexacelsian-like phase (Cs-HEX). Errors in pressure and temperature measurements

347   are estimated to be ±0.1 GPa and $\pm10°C$, respectively. (b) Changes in the calculated

348   density (g/cm^3) per Cs atoms ($\times$ 1000) in a unit volume (1 $Å^3$).

349

350   **Figure 3.** Polyhedral representations of the successive transformations from the

351   dehydrated Cs-exchanged natrolite (deh-Cs-NAT), the ordered hydrated natrolite (Cs-

352   NAT-II), the H_2O-free pollucite-like phase (anh-Cs-POL), and to the hexacelsian-like

353   phase (Cs-HEX). Red and yellow circles represent H_2O molecules and Cs^+ extra-

354   framework cations, respectively. Two-toned polyhedra in the natrolite framework

355   illustrate the ordered arrangements of the Si- and Al-tetrahedra.

356

357   **Figure 4.** Crystal structure of the hexacelsian-like phase (Cs-HEX) com-pared to the Ba-

358   hexacelsian by Kremenovic et al. (2003). Upper and lower figures are views along and

16

359   perpendicular to the c-axis, respectively.   Cation-to-oxygen coordination distances are

360   illustrated with two separate bars for long- and short-bonds.

361

362   **Figure 5.** HAADF-STEM images from a recovered Cs-HEX particle viewed down [001].

363   A tetrahedral representation of the refined Cs-HEX structure is overlain on the

364   experimental HAADF-STEM image to show the match between the Z-contrast and the

365   distribution of the Cs^+ extra-framework cations in the model.

366

17

367   **Table 1.** Pressure- and heat-induced changes in the unit-cell volume, normalized to 80

368   framework oxygen atoms ($80O_f$) from the dehydrated Cs-exchanged natrolite (deh-Cs-

369   NAT), the ordered hydrated natrolite (Cs-NAT-II), the H_2O-free pollucite-like phase

370   (anh-Cs-POL), and to the hexacelsian-like phase (Cs-HEX).   Errors in pressure and

371   temperature measurements are estimated to be ±0.1 GPa and ±10°C, respectively.

372

Phase	Pressure (GPa)	Temperature treatment (°C)	Volume per $80O_f$ ($Å^3$)
deh-Cs-NAT	0.0001		2235.6(3)
	0.5(1)		2197.5(3)
Cs-NAT-II	0.5(1)	100	2503.0(2)
	0.8(1)		2475.5(3)
	0.8(1)	120	2473.3(2)
	1.3(1)		2432.7(2)
	1.3(1)	140	2437.9(2)
	1.5(1)		2416.4(1)
	1.5(1)	145	2413.4(2)
	2.0(1)		2393.6(2)
anh-Cs-POL	1.5(1)	145	2039.3(2)
	2.0(1)		2018.2(2)
	2.6(1)		1992.2(2)
	2.6(1)	165	1988.3(2)
	3.7(1)		1942.3(2)
Cs-HEX	3.7(1)	180	1907.2(1)
	4.3(1)		1894.3(5)
	4.3(1)	190	1880.5(2)
	1.0(1)		2028.9(2)
	0		2085.6(2)

373

374

375

376

377

378

18

379 **Table 2.** Crystal data and details pertaining to the structure refinements of the

380 hexacelsian-like phase (Cs-HEX) compared to those of the Ba-hexacelsian by

381 Kremenovic et al. (2003).

382

	Cs-HEX (released)	Cs-HEX (3.7 GPa, 180 °C)	Cs-HEX (4.3 GPa, 190 °C)	Ba-HEX
Unit-cell formula		$Cs_{1.547}Al_{1.548}Si_{6.452}O_{16}$		$Ba_2Al_4Si_4O_{16}$
Formula weight		684.55		750.91
Space group		$P6_3/mcm$		$P6_3/mcm$
Unit-cell dimension (Å)	$a = 5.3731(2)$ $c = 16.6834(8)$	$a = 5.3275(1)$ $c = 15.5180(5)$	$a = 5.3172(2)$ $c = 15.3606(7)$	$a = 5.2920(4)$ $c = 15.557(2)$
Unit-cell Volume($Å^3$)	417.12(4)	381.43(2)	376.10(3)	377.308
Calculated density(g/cm^3)	2.725	2.980	3.022	3.306
Parameters reduced χ^2	15.87	3.563	3.533	
R_{wp}(%)	5.42	6.64	7.17	

383

384

385

386

387

388

389

390

391

392

393

19

394 **Table 3.** Refined atomic positional, occupancy, and displacement parameters of the

395 hexacelsian-like phase (Cs-HEX) compared to those of the Ba-hexacelsian by

396 Kremenovic et al. (2003). Estimated standard deviations are in parenthesis.

397

398

		Cs-HEX (release)	Cs-HEX (3.7 GPa, 180 °C)	Cs-HEX (4.3 GPa, 190 °C)			Ba-HEX
T 8h	x	1/3	1/3	1/3	T 8h	x	1/3
	y	2/3	2/3	2/3		y	2/3
	z	0.150(1)	0.145(1)	0.144(1)		z	0.145(2)
	occu. Al/Si	0.1935 / 0.8065	0.1935 / 0.8065	0.1935 / 0.8065		occu.	0.5/0.5
	U_{iso}	0.015(1)	0.015	0.015		U_{iso}	0.01140
O1 4c	x	1/3	1/3	1/3	O1 4c	x	1/3
	y	2/3	2/3	2/3		y	2/3
	z	1/4	1/4	1/4		z	1/4
	occu.	1.0	1.0	1.0		occu.	1.0
	U_{iso}	0.015(1)	0.015	0.015		U_{iso}	0.01267
O2 12k	x	0.498(2)	0.489(1)	0.498(1)	O2 12k	x	0.489(3)
	y	0	0	0		y	0
	z	0.117(1)	0.110(1)	0.108(1)		z	0.104(2)
	occu.	1.0	1.0	1.0		occu.	1.0
	U_{iso}	0.015(1)	0.015	0.015		U_{iso}	0.04559
Cs 2b	x	0	0	0	Ba 2b	x	0
	y	0	0	0		y	0
	z	0	0	0		z	0
	occu.	0.773(6)	0.773	0.773		occu.	1
	U_{iso}	0.015(1)	0.015	0.015		U_{iso}	0.02026

20

399   **Table 4.** Selected interatomic distances (Å) and angle (o) of the hexacelsian-like phase

400   (Cs-HEX) compared to those of the Ba-hexacelsian by Kremenovic et al. (2003).

401   Estimated standard deviations are in parenthesis.

402

|	Cs-HEX (released)	Cs-HEX (3.7 GPa, 180 °C)	Cs-HEX (4.3 GPa, 190 °C)		Ba-HEX
T-O1	1.663(1)	1.634(1)	1.635(1)	T-O1	1.642
T-O2	1.649(1) × 3	1.630 (1) × 3	1.631(1) × 3	T-O2	1.652 × 3
O1-O2	2.710(1)	2.661(3)	2.672(3)	O1-O2	2.738
O2-O2	2.687(1)	2.666(1)	2.659(1)	O2-O2	2.678
Cs-O2	3.326(1) × 6 3.311(1) × 6	3.215(6) × 6 3.115(5) × 6	3.141(4) × 6 3.120(4) × 6	Ba-O2	3.052 × 6 3.151 × 6
T-O1-T	180.0	180.0	180.0	T-O1-T	180
T-O2-T	140.3(1)	141.4(2)	140.4(2)	T-O2-T	135
Distance between T-layer	3.897(1)	3.421(7)	3.306(6)	Distance between T-layer	3.238

403

404

405

406

407

408

409

410

411

412

413

21

414

415   **Figure 1**

22

416
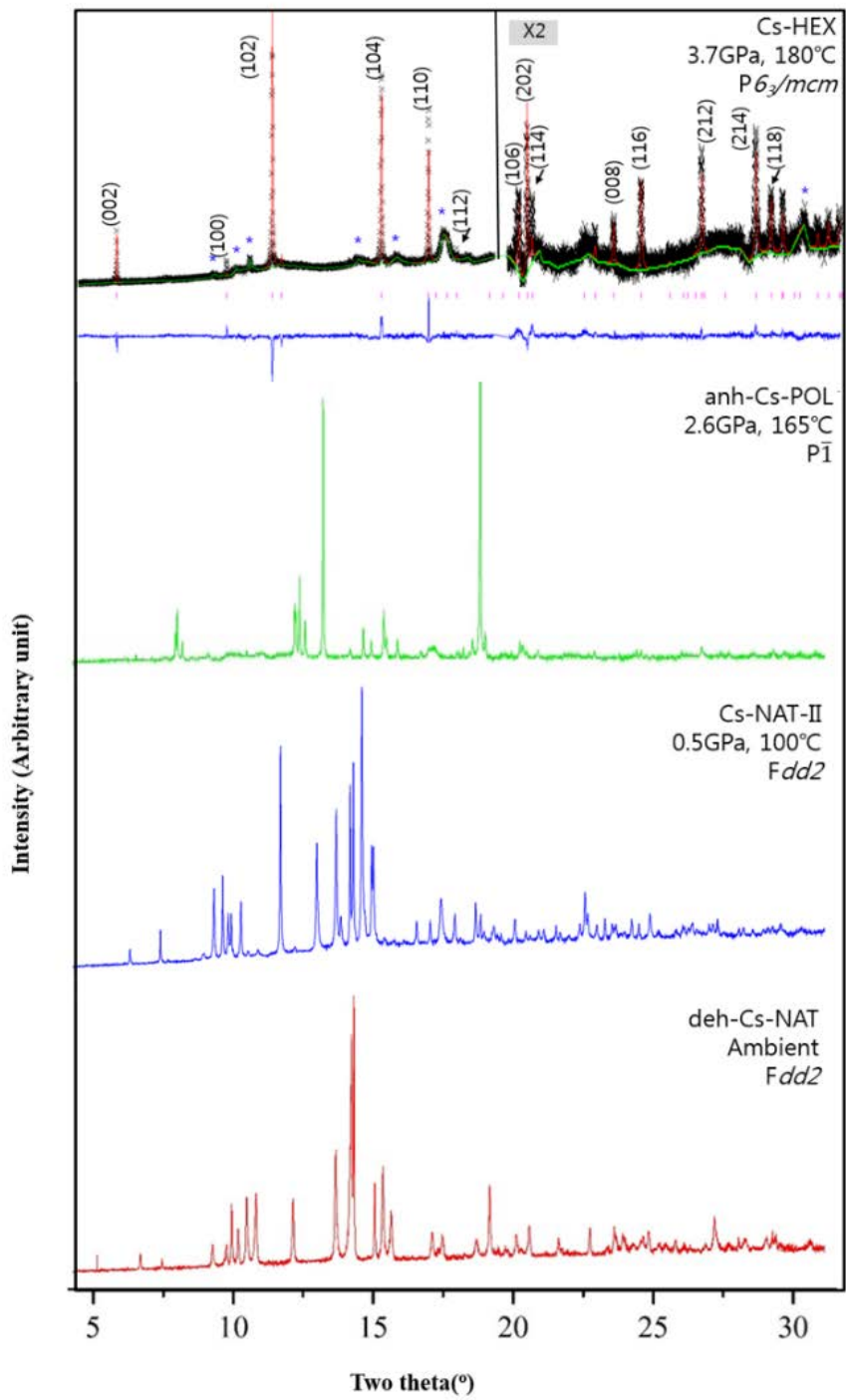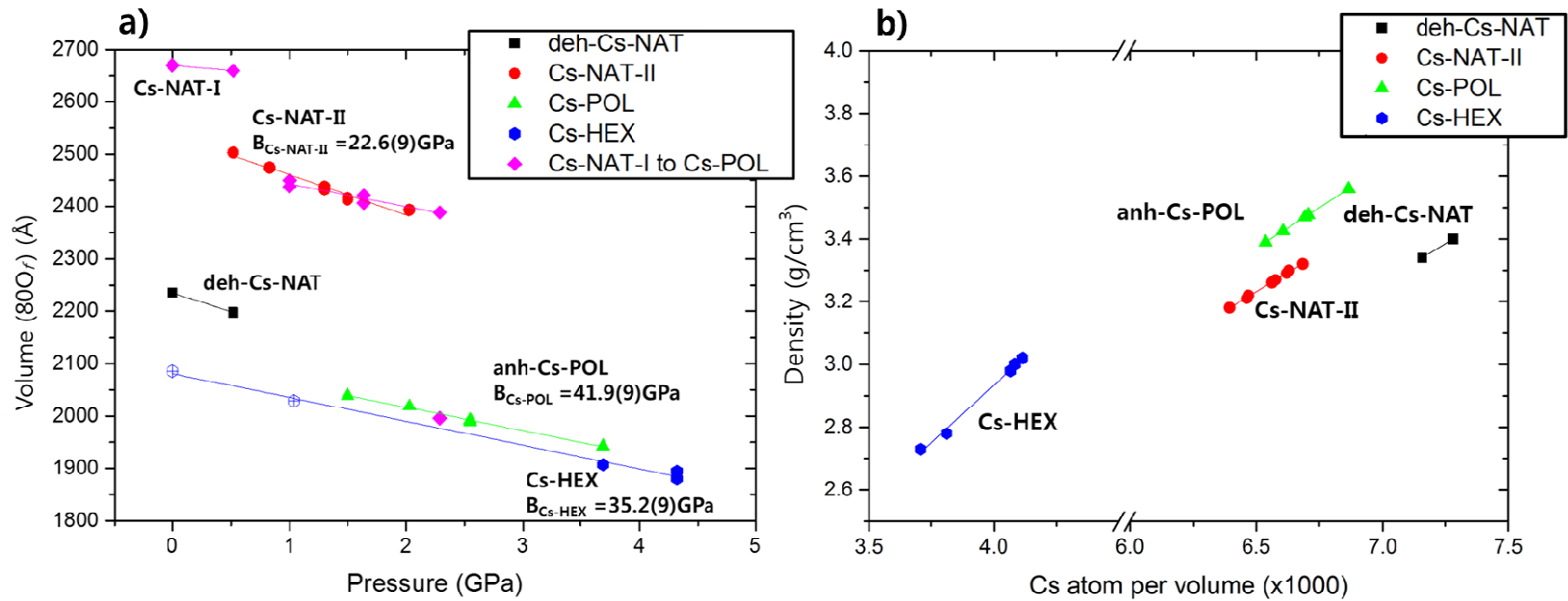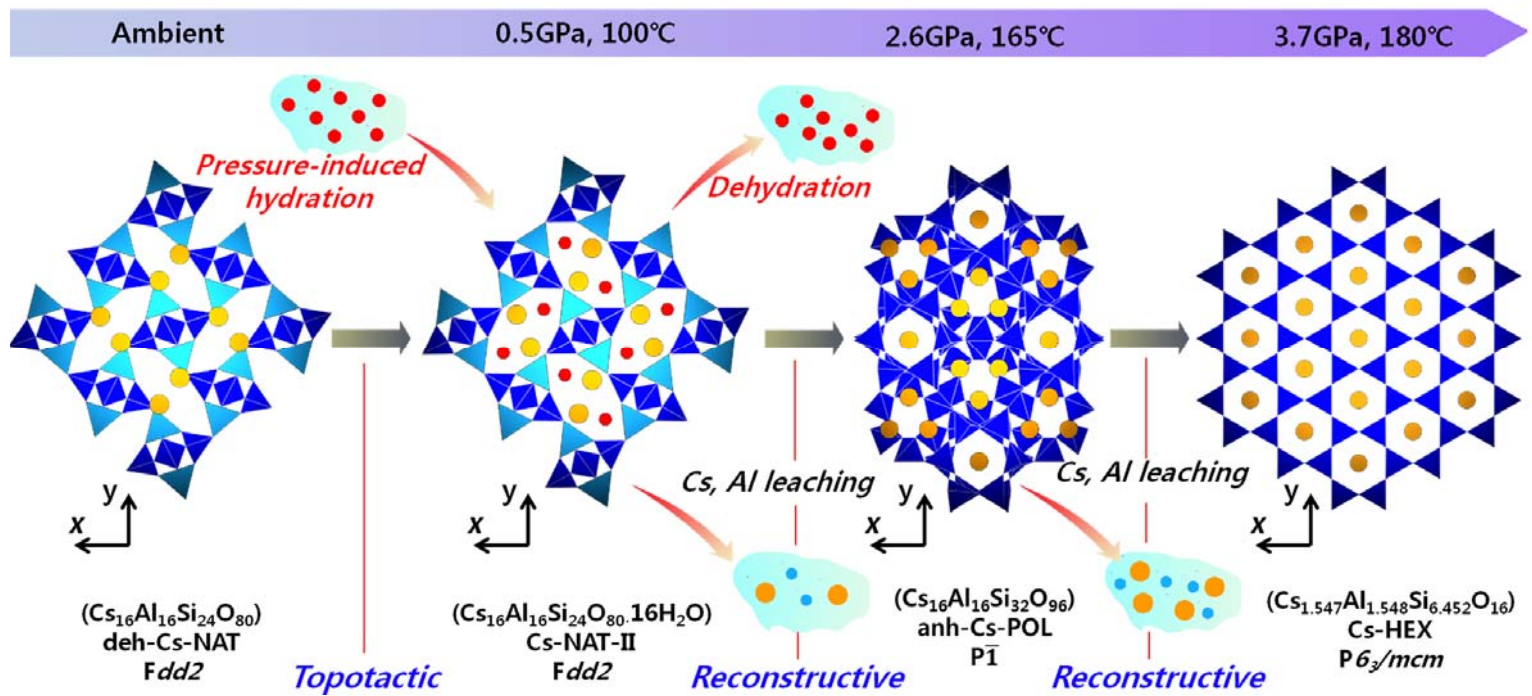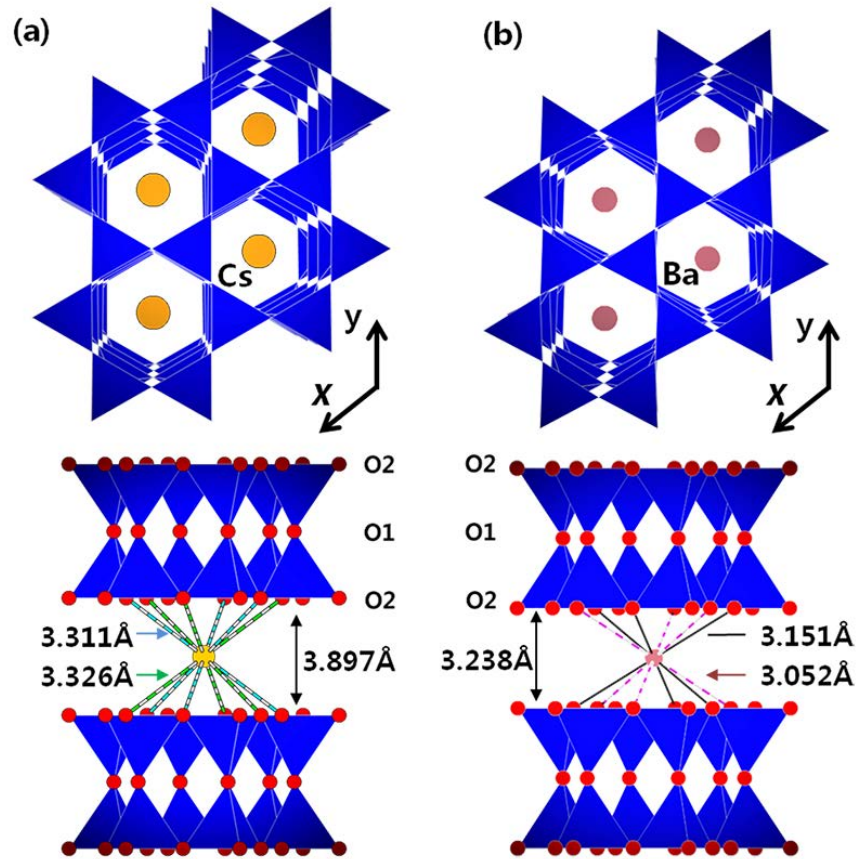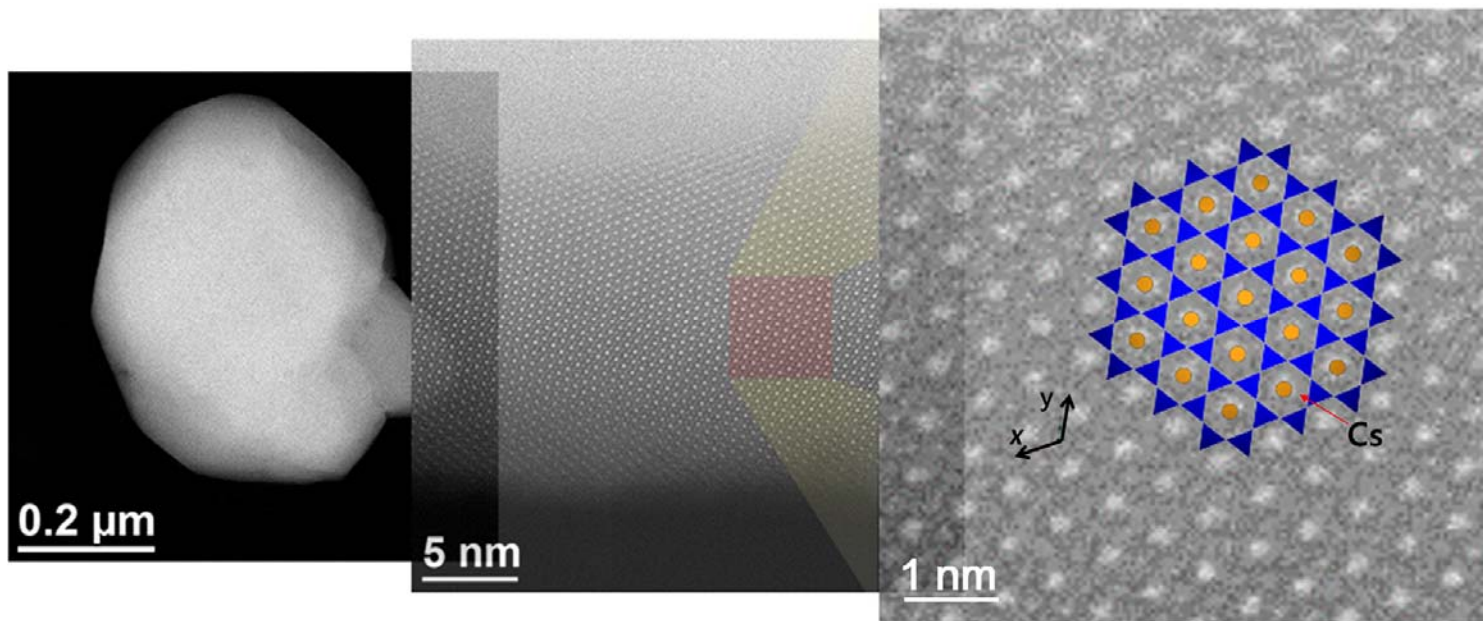
Figure 2

418

419

420

Figure 3

421

422

423

24

424

425　**Figure 4**

426

427   **Figure 5**

26